lubricants

MDPI

Article

Effect of Quenching Temperature on Microstructure and Wear Resistant Properties of Mo_2FeB_2 Cermet Coating

Hao Zhang [1], Yongqi Hu [1] and Yang Zhang [2,*]

[1] College of Optoelectronic Manufacturing, Zhejiang Industry & Trade Vocational College, Wenzhou 325003, China; zhanghao573@163.com (H.Z.)
[2] School of Engineering + Technology, Western Carolina University, Cullowhee, NC 28723, USA
* Correspondence: yzhang@wcu.edu

Abstract: H13 steel, a widely used material in hot work tooling, faces premature failure due to insufficient hardness and wear resistance. To address this limitation, Mo_2FeB_2 cermet coatings were fabricated on H13 alloy steel via plasma spray welding, and subsequently quenched at 850 °C, 1000 °C, and 1150 °C. The effects of the quenching temperature on the microstructure and wear resistance were investigated using optical microscopy (OM) for cross-sectional morphology, scanning electron microscopy (SEM) for microstructural and wear surface analyses, energy-dispersive spectroscopy (EDS) for elemental composition analysis, and X-ray diffraction (XRD) for phase identification. The coating primarily consisted of α-Fe, Mo_2FeB_2, $(Mo,Fe,Cr)_3B_2$, and $Fe_{23}(B,C)_6$ phases. Increasing the temperature to 1150 °C increased the Mo_2FeB_2 hard phase and elevated microhardness by 32.04% (from 827 $HV_{0.5}$ to 1092 $HV_{0.5}$). Wear resistance improved by 46.38% (mass loss reduced from 6.9 mg to 3.7 mg). The main wear mechanism was identified as abrasive wear due to the spalling of hard phase particles. These results demonstrate that optimizing quenching temperature enhances the hardness and wear resistance in Mo_2FeB_2 coatings, offering a viable strategy to extend H13 steel service life in high-temperature industrial applications.

Keywords: plasma spray welding; Mo_2FeB_2; quenching temperature; microstructure; wear resistance

check for updates

Received: 23 April 2025
Revised: 14 May 2025
Accepted: 21 May 2025
Published: 23 May 2025

Citation: Zhang, H.; Hu, Y.; Zhang, Y.. Effect of Quenching Temperature on Microstructure and Wear Resistant Properties of Mo_2FeB_2 Cermet Coating. *Lubricants* **2025**, *13*, 233. https://doi.org/10.3390/lubricants13060233

Copyright: © 2025 by the authors. Licensee MDPI, Basel, Switzerland. This article is an open access article distributed under the terms and conditions of the Creative Commons Attribution (CC BY) license (https://creativecommons.org/licenses/by/4.0/).

1. Introduction

With the rapid development of the molding industry, mold materials have advanced significantly [1]. Among these, H13 steel has emerged as one of the most widely used materials due to its strong carbide-forming elements (Cr, Mo, and V), excellent toughness [2], high hardenability [3], and resistance to heat softening [4]. These properties make it suitable for applications such as non-ferrous metal die casting, hot extrusion, hot forging, and plastic molding [2,5]. However, H13 steel often fails to meet the demands of harsh working conditions due to its softness (~202–241 HV) [6]; limited wear resistance; and vulnerability to thermal fatigue [5], erosion, and stress corrosion [2].

Many large-scale engineering components operate in harsh environments involving water vapor, liquids, and solid particles, which leads to severe corrosion and wear, ultimately resulting in premature failure. The surface remanufacturing techniques offer an effective solution by restoring and enhancing the performance of damaged or worn regions. To extend H13's service life, various surface modification techniques have been explored. Meng et al. [7] studied the mechanical properties of TiC-reinforced H13 steel fabricated via bionic laser treatment. The results showed that with an increasing TiC fraction, the microstructure of the laser alloying zone was refined, and the microhardness was

improved to 1156 HV when the TiC fraction was 70%. However, tensile strength and wear resistance initially increased before declining at higher TiC fractions. Narvan et al. [8] investigated the feasibility of fabricating defect-free functionally graded bi-materials (FGMs) by incorporating vanadium carbide (VC) into H13 tool steel to enhance wear resistance. They found that the microhardness values of 1, 3 and 5 wt% VC were 700, 785, and 840 HV, respectively. The nanoindentation maximum penetration depth decreased to 515, 489, and 470 nm, respectively. Ref. [9] investigated the microhardness, wear properties, and microstructure of Fe-based coatings containing various WC contents deposited on H13 die steel via laser cladding. The results demonstrated that the coating microhardness increased with higher WC particle mass fractions. The average COFs of the coatings with 0%, 3%, 6%, and 9% were 0.349, 0.342, 0.336, and 0.313, respectively. The wear rates were 4.3326, 3.9476, 3.3240, and 2.7194 $\times$ 10^{-6} $mm^3 \cdot N^{-1} \cdot m^{-1}$, respectively.

Among the surface modification methods, plasma spray welding offers distinct advantages: a fine heat-affected zone, strong metallurgical bonding at the coating–substrate interface, minimal porosity, and high coating thickness [10,11]. In this work, plasma spray welding was employed to deposit in situ Mo_2FeB_2-based cermet coatings on H13 steel, followed by quenching at varying temperatures to further enhance the performance. Compared to alternatives like Mo_2NiB_2 [12,13] and WCoB [14,15], Mo_2FeB_2-based cermets are cost-effective, while retaining hardness, chemical stability, and wear resistance, making them suitable for tools, cladding materials, and industrial components [16–18]. However, prior research on Mo_2FeB_2 cermets has primarily focused on sintering [19,20] or non-heat-treated cladding [21], leaving their post-deposition heat treatment underexplored.

Quenching is a rapid heat and mass transfer process where a high-temperature surface is rapidly cooled by a fluid below its boiling point [22,23]. Appropriate heat treatment not only defines the coating's microstructure, relieving residual stresses, promoting crystallization, and enhancing mechanical properties, but can also alter its phase composition and morphology [24–26].

In this study, coatings containing Mo_2FeB_2 hard phase were deposited on H13 tool steel by plasma spray welding, and then quenched at various temperatures. The effects of the quenching temperature on the coating morphology, phase composition (XRD), microhardness, microstructure, and wear resistance were systematically investigated. The primary objective is to demonstrate that the combined use of plasma spray welding and optimized quenching can substantially improve the hardness and wear resistance of H13 steel, thereby extending its service life and reducing the overall tooling costs. By depositing a Mo_2FeB_2 coating on the material surface, the limitations of metallic materials in terms of insufficient hardness and poor wear resistance can be effectively addressed. At the same time, the brittleness of ceramic materials and the interfacial incompatibility between ceramics and metallic substrates can be mitigated.

2. Materials and Methods

2.1. Materials

An H13 alloy steel substrate (50 $\times$ 30 $\times$ 10 mm^3) was used in this study, with its elemental composition provided by the manufacturer shown in Table 1. Prior to the experiments, the H13 substrates were prepared by polishing the surface to a roughness of Ra < 1.0 μm, followed by ultrasonic cleaning in alcohol for 20 min. The cleaned substrates were then preheated in a heat treatment furnace at 300 °C for 10 min to remove residual moisture. Plasma spray welding powder consisted of Mo (3–5 μm), FeB (8–10 μm, 19.7 wt.% B), carbonyl Fe (2–3 μm), Cr (5–8 μm), Ni (1–5 μm), and SiC (1–2 μm) powders (chemical composition provided by the manufacturer shown in Table 2). Before deposition, the powders were premixed and ball-milled using a QM-1SP4 planetary ball milling ma-

chine. Milling was performed with cemented carbide vials and balls (10 mm diameter) at a ball-to-powder weight ratio of 5:1. The mill ran at 300 rpm for 24 h, with absolute ethanol added as a process control agent. After milling, the powder was dried at 200 °C for 2 h in a drying oven.

Table 1. Elemental composition (wt.%) of H13 alloy steel.

C	Si	Mn	Cr	Mo	V	P	S	Fe
0.35~0.40	1.13~1.20	0.40~0.50	4.50~4.80	1.30~1.50	0.80~1.00	≤0.03	≤0.03	Rest

Table 2. Elemental composition (wt.%) of plasma spray welding powder.

Mo	FeB	Cr	SiC	Ni	Fe
18~25	10~15	5~8	0.3~0.6	1~1.5	Rest

2.2. Experimental Procedure

Plasma spray welding was performed using a DPT100 welding gun, 400A plasma current, and an MDS-3 powder feeder (United Coatings Technologies Co., Ltd., Beijing, China). Detailed process parameters are summarized in Table 3.

Table 3. Process parameters of plasma spray welding.

Nozzle Height (mm)	Voltage (V)	Non-Transferred Arc (A)	Transferred Arc (A)	Plasma Ar Gas Flow (L/min)	Powder Ar Gas Flow (L/min)	Powder Feeding (g/min)	Surfacing Speed (mm/min)
10	30	11	90	1.0	4	10	80

After spray welding, the samples were heat-treated in an SX-4-10 furnace at a rate ≤ 400 °C/h, followed by a 30 min hold. The samples were categorized based on heat treatment: C0 (no heat treatment), C1 (heated to 850 °C), C2 (heated to 1000 °C), and C3 (heated to 1150 °C). Quenching temperatures of 850 °C, 1000 °C, and 1150 °C were selected based on the high-temperature characteristics of the primary hard phase Mo_2FeB_2. These elevated temperatures were chosen to promote the re-nucleation and refinement of new Mo_2FeB_2 particles during the heat treatment process. Samples C1, C2, and C3 were quenched in mineral oil after reaching their target temperatures. For characterization, all the samples were cut to 10 mm × 10 mm × 5 mm, ground, and polished. The polished surfaces were then etched for 20 s in a solution containing $K_3[Fe(CN)_6]$, NaOH, and H_2O (volume ratio 1:1:10), followed by ultrasonic cleaning in alcohol.

2.3. Characterization

The cross-sectional microstructure of the coatings was examined using a ZEISS Axio Plan 2 optical microscope (OM) (Zeiss, Shanghai, China). Phase composition analysis was performed via X-ray diffraction (XRD) (PANalytical, Almelo, The Netherlands) on an X'Pert Pro MPD system with Cu Kα radiation (λ = 0.15418 nm) operated at 40 kV and 20 mA. Scans were conducted over a 2θ range of 10–90° with a step size of 0.05° and a dwell time of 10 s per step. Wear morphology and microstructure were characterized using a field-emission scanning electron microscope (FE-SEM, Nova 400 Nano, FEI, Hillsboro, OR, USA) equipped with an energy-dispersive X-ray spectroscopy (EDS) (INCA IE 350 PentaFETX-3, Oxford, UK) system for elemental analysis. Microhardness was measured on polished cross-sections using an HX-500 microhardness tester (Laizhou Yutong Test Instrument Co. Ltd., Laizhou, Shandong, China) under 500 g force load applied for 10 s. To ensure the accurate characterization of the transition region, microhardness measurements were conducted more densely near the interface, specifically at 50 μm intervals above

and below the fusion line. Wear resistance was evaluated under dry sliding conditions with a UMT-TriboLab tribometer (Bruker, Billerica, MA, USA). A Si_3N_4 ball (cemented carbide, 2200 $HV_{0.5}$) served as the counterface. The tests were run at a normal load of 100 N, a reciprocating frequency of 5 Hz, and a total duration of 1 h. For each condition, the average coefficient of friction and mass loss were determined from three replicate tests; mass loss was measured with an electronic balance.

3. Results and Discussion

3.1. Coating Morphology

Figure 1 shows the cross-sectional microstructure of the coating, where the thickness of the coating is approximately 575 µm. In Figure 1a, a large number of hard phase particles (black) are embedded in the binder phase (white). Some regions show the noticeable agglomeration of these hard phase particles. This agglomeration is attributed to the short duration of the plasma spray welding process, which limited the time available for the formation of a liquid molten pool and resulted in a rapid solidification rate. As a consequence, the hard phase particles were distributed unevenly within the binder; the middle region of the coating exhibited more pronounced agglomeration, whereas such clustering was almost absent in the fusion zone between the coating and the substrate. In the fusion zone, the high-energy thermal cycle extended the high-temperature duration near the molten pool, allowing for the hard phase particles sufficient time to react and diffuse, thereby reducing the tendency for agglomeration.

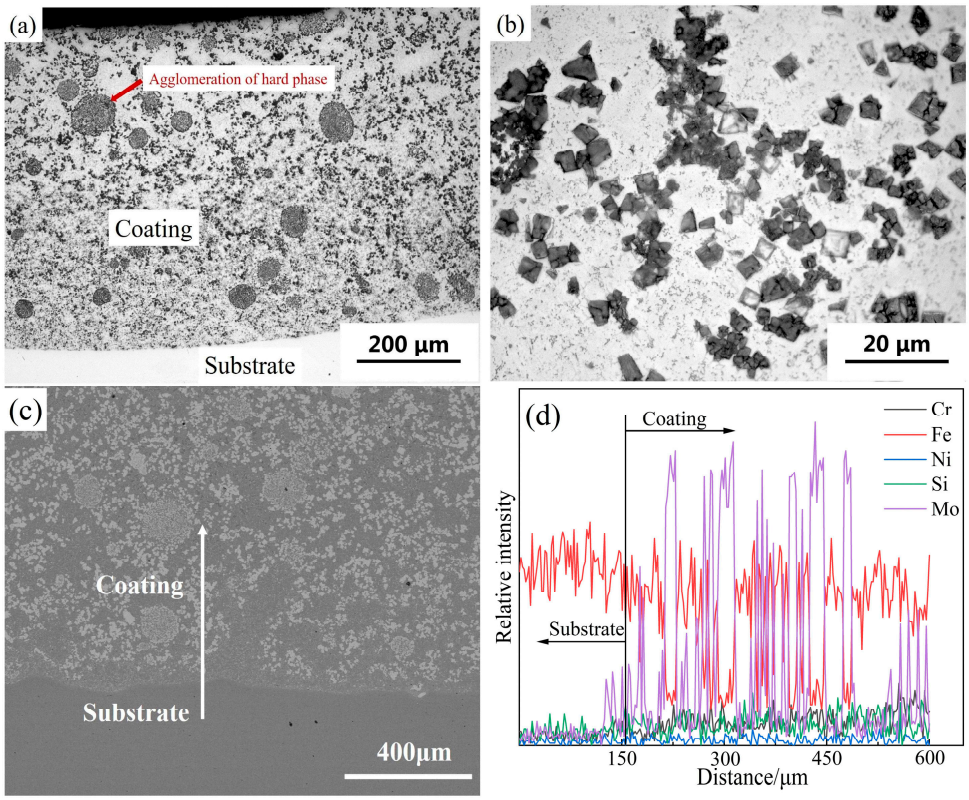

Figure 1. The cross-section of the coating. (**a**) The OM morphology of the bonding zone; (**b**) the OM morphology of the coating; (**c**) the SEM morphology of the bonding zone; (**d**) an EDS line scan in the marked area of (**c**).

Figure 1b reveals that the coating is composed of three distinct phases: a binder phase, a hard phase, and a eutectic structure. Interfacial bonding between the coating and the

substrate is further examined in Figure 1c, which demonstrates a strong metallurgical bond with no visible defects, such as pores, inclusions, and cracks.

The EDS line scan result in Figure 1c is shown in Figure 1d, indicating significant changes in the contents of Mo, Fe, and Cr from the substrate to the coating. Notably, there is considerable fluctuation in the Mo and Fe concentrations on both sides of the interface. This variation is attributed to the interdiffusion of elements during the high-energy welding process, with Mo from the coating diffusing into the substrate and Fe from the substrate diffusing into the coating. Overall, the Mo and Cr contents are considerably lower in the substrate compared to the coating, while the Fe content is higher in the substrate. These EDS results confirm the existence of strong metallurgical bonding between the coating and the substrate.

3.2. XRD Analysis

Figure 2 shows the XRD patterns of the coatings subjected to different quenching temperatures. The C0 coating consists of α-Fe, Mo_2FeB_2, $(Mo,Fe,Cr)_3B_2$, and $Fe_{23}(C,B)_6$. After high-temperature quenching (C2: 1000 °C; C3: 1150 °C), the $Fe_{23}(C,B)_6$ phase disappears, while the diffraction peak intensities of Mo_2FeB_2 and $(Mo,Fe,Cr)_3B_2$ increase significantly. This indicates that elevated temperatures (≥1000 °C) promote the dissolution of $Fe_{23}(C,B)_6$ and enhance the formation of Mo_2FeB_2 and $(Mo,Fe,Cr)_3B_2$.

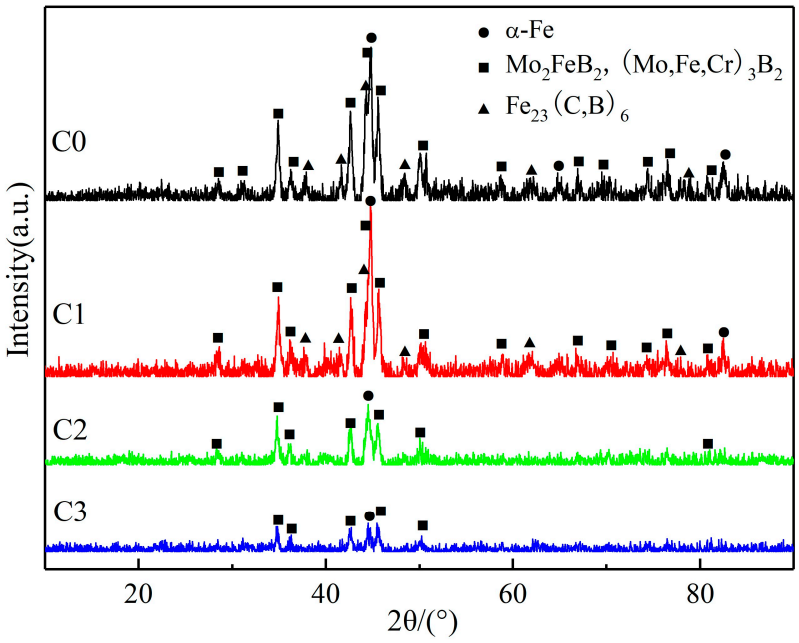

Figure 2. XRD patterns of boride coating with different quenching temperatures.

During the formation of the Mo_2FeB_2 hard phase, a portion of the Cr atoms replaces the Mo or Fe atoms [21], leading to the formation of $(Mo,Fe,Cr)_3B_2$. This substitution induces lattice distortion in the Mo_2FeB_2 crystals, which is beneficial for enhancing the coating's hardness [21]. In addition, the presence of the α-Fe binder phase effectively improves the plasticity of the coating. The eutectic structure consists of (α-Fe + $Fe_{23}(B,C)_6$). During the rapid cooling of the molten pool, grain boundaries serve as channels for rapid atomic diffusion, promoting the segregation of impurity atoms. Elements such as C and B diffuse and precipitate along these boundaries, forming $Fe_{23}(B,C)_6$, which then reacts with α-Fe to produce the eutectic structure.

3.3. Microstructure

Figure 3 shows the SEM morphologies of the hard phases in the coatings subjected to different quenching temperatures. The in situ Mo_2FeB_2 and $(Mo,Fe,Cr)_3B_2$ hard phases retained similar morphologies across all the samples, though their volume fraction increased with higher quenching temperatures. As the quench temperature rose, finer white hard phase particles gradually appeared within the coating. The average grain size of the coatings was measured using Image-Pro Plus, and the values are approximately 18.78 μm, 9.88 μm, 9.70 μm, and 9.48 μm for C0, C1, C2, and C3, respectively. In contrast, the binder phase and the reticulated eutectic network undergo pronounced morphological changes, in agreement with the XRD findings (Figure 2). To examine these transformations more closely, Figure 4 and Table 4 summarize the EDS point analyses of representative regions.

In the C0 coating, reticulated eutectic structures (point 2) were observed. At 850 °C (C1), these structures break up, yielding elongated or rod-like boride phases (point 4). Further increasing the temperature to 1000 °C (C2) and 1150 °C (C3) promoted the formation of fine hard phase particles (points 6 and 8) within the binder. EDS analysis (Table 4) revealed a Mo/Fe/Cr atomic ratio of ~(5–5.5):3:1, confirming the hard phases as Mo_2FeB_2 and $(Mo,Fe,Cr)_3B_2$. The disappearance of the eutectic structure at high quench temperatures (1000 °C and 1150 °C) indicates that Mo from the binder reacts with B from the eutectic structure to form new boride particles, which then grow into granular or spherical shapes. With increasing temperature, these particles coarsen and become more evenly distributed.

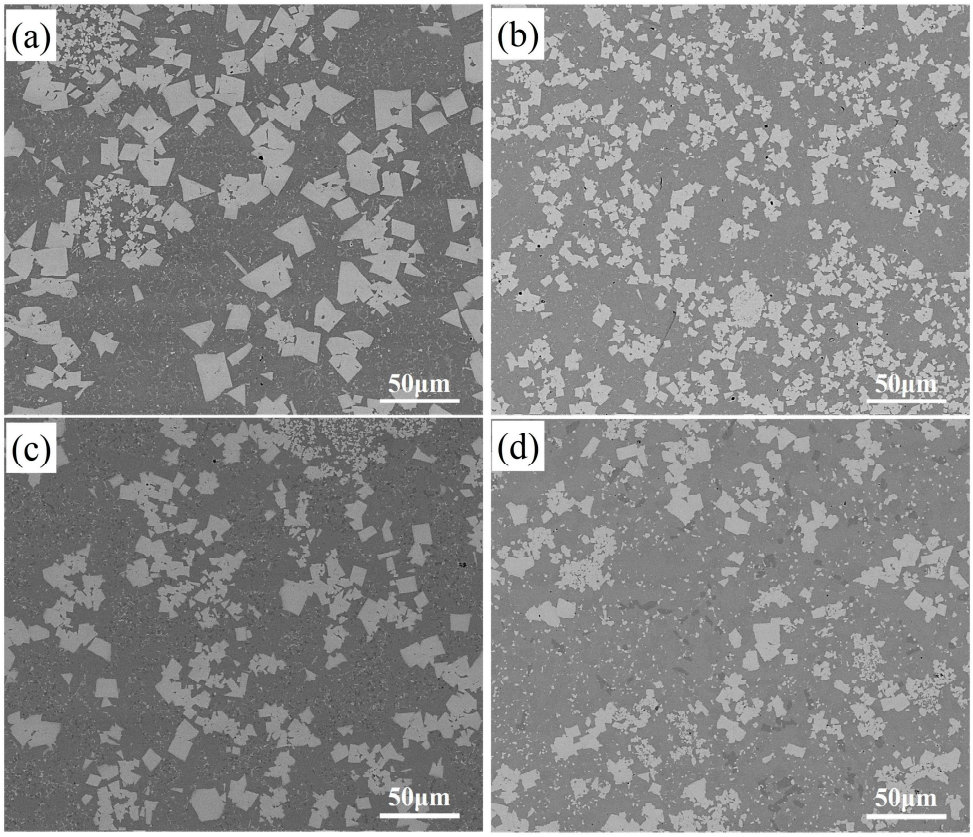

Figure 3. SEM morphologies of hard phases in coating at different quenching temperatures (**a**) C0; (**b**) C1; (**c**) C2; and (**d**) C3.

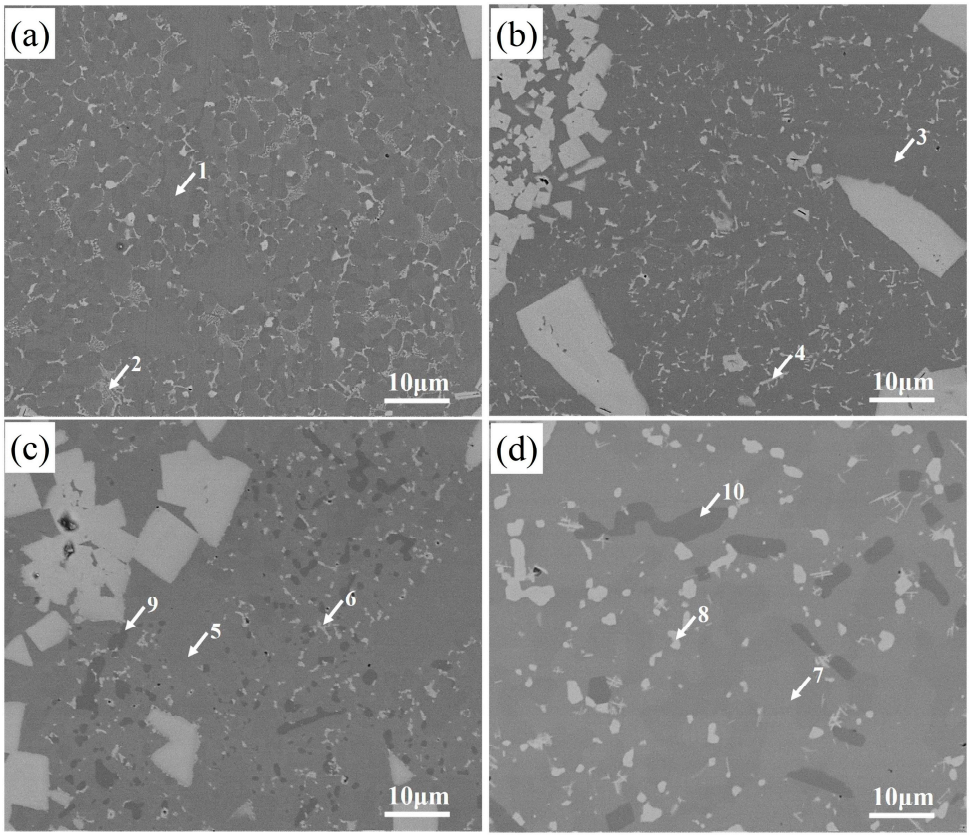

Figure 4. SEM morphologies of binder phases in coatings at different quenching temperatures (**a**) C0; (**b**) C1; (**c**) C2; and (**d**) C3.

Table 4. EDS analysis results of marked points in Figure 4.

Point	Weight%					Atomic%				
	Mo	Fe	Cr	Ni	Si	Mo	Fe	Cr	Ni	Si
1	1.13	41.03	1.97	3.10	1.51	0.96	83.10	3.87	5.97	6.10
2	13.00	7.64	2.57	0.78	0.27	39.30	39.67	14.35	3.88	2.80
3	1.41	57.20	2.28	4.01	1.94	1.19	83.24	3.92	5.56	6.08
4	24.93	32.26	3.05	1.67	1.01	26.97	59.91	6.09	2.94	4.09
5	-	52.01	1.69	3.87	3.41	-	80.88	2.83	5.73	10.56
6	38.95	15.34	5.65	-	-	51.43	34.81	13.76	-	-
7	-	53.68	2.04	4.01	2.56	-	82.57	3.73	5.87	7.83
8	41.47	14.68	5.42	-	-	54.07	32.88	13.05	-	-
9	-	45.92	7.95	-	-	-	84.32	15.68	-	-
10	-	46.61	7.34	-	-	-	85.53	14.47	-	-

The EDS points in the binder phase (points 1, 3, 5, and 7) represent Fe along with Cr, Ni, and Si, elements known to stabilize ferrite and provide solid-solution strengthening. In C1, the binder composition is similar to C0, indicating limited diffusion at 850 °C. In C2 and C3, however, Mo originally dissolved in the binder reacts fully to form additional Mo_2FeB_2, while Cr incorporates into Mo_2FeB_2 lattices to form $(Mo,Fe,Cr)_3B_2$ [19]. Notably, the darker binder regions (points 9 and 10) appear in C2 and C3, composed exclusively of Fe and Cr. At quench temperatures $\geq$ 1000 °C, Ni and Si (which do not participate in Mo_2FeB_2 formation) were excluded from the reaction front. Rapid quenching trapped these elements in a depleted area, leaving localized Fe-Cr binder domains upon cooling.

3.4. Microhardness

Figure 5 shows the microhardness distributions of the coatings quenched at different temperatures. The microhardness values across each coating were relatively uniform, with no significant fluctuations. The average microhardness values of samples C0, C1, C2, and C3 were 827 $HV_{0.5}$, 905 $HV_{0.5}$, 1061 $HV_{0.5}$, and 1092 $HV_{0.5}$, respectively. Compared with C0, the microhardness of C1, C2, and C3 increased by 9.43%, 28.29%, and 32.04%, respectively.

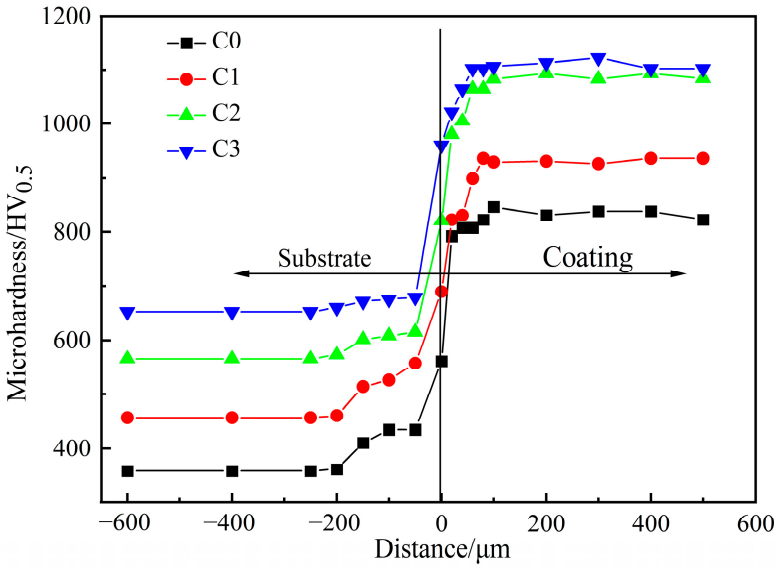

Figure 5. Microhardness distribution at different quenching temperatures.

The observed hardness enhancement is closely related to the microstructural evolution during quenching. After high-temperature quenching (C2 and C3), the reticulated eutectic structure disappeared, and the coating had sufficient thermal energy and time to undergo in situ phase transformations. This promoted the formation of a larger quantity of Mo_2FeB_2 hard phase particles. These boride particles significantly contributed to increased hardness. Therefore, it can be inferred that both the disappearance of the eutectic structure and the generation of hard phase particles have a strong influence on the coating's microhardness.

3.5. Wear Resistance

Figure 6 shows the variation in the coefficient of friction (COF) of the coatings at different quenching temperatures. The COF curves of C0 and C1 exhibit significant fluctuations as wear time increased, indicating poor wear resistance. This can be attributed to the rapid heating and cooling cycles inherent in plasma spray welding, which result in uneven residual stress distribution within the coating. For the C0 sample, which did not undergo any heat treatment, residual stress was not relieved. This led to stress concentrations and the formation of microcracks during the wear process, thereby causing large fluctuations in the COF. In addition, due to the relatively low microhardness of the C0 coating compared to the friction counterpart, substantial wear debris was generated, further accelerating wear and increasing the COF over time. For the C1 sample, although heat-treated at 850 °C with 30 min of holding time followed by quenching in mineral oil (a medium with good cooling efficiency), residual stress was only partially released [27]. The resulting decrease in lattice distortion contributed to a slight reduction in the COF compared with that of C0. However, because 850 °C was insufficient to fully relieve internal stresses, some fluctuation in the COF curve still remains.

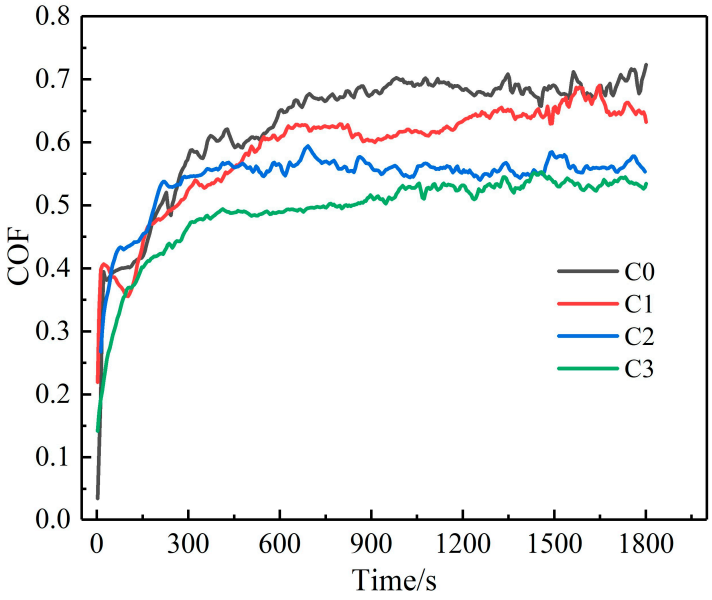

Figure 6. Variation in coefficient of friction of coatings at different quenching temperatures.

In contrast, after high-temperature quenching (C2 and C3), the COF curves showed a much flatter trend with increasing wear time, indicating improved wear stability. The enhanced wear resistance at higher quenching temperatures was associated with the progressive disappearance of eutectic structures (as seen in Figure 4) and the increased formation of Mo_2FeB_2 hard phase particles. These microstructural changes strengthened the coating and reduced its wear rate. Furthermore, residual stress was more effectively relieved at higher quenching temperatures, contributing to the coating's enhanced wear performance. Overall, the C3 coating demonstrated the best wear resistance, as evidenced by the most stable COF curve during the wear process.

Figure 7 shows the variation in the average COF and mass loss of the coatings at different quenching temperatures. The average COF decreased progressively from C0 to C3. The wear mass loss data represent the average values obtained from three repeated measurements to ensure reliability. The mass losses of samples C0, C1, C2, and C3 were 6.9 mg, 5.7 mg, 4.0 mg, and 3.7 mg, respectively. Under similar wear test conditions, the wear mass losses of C1, C2, and C3 decreased by 17.4%, 42.03%, and 46.38% compared with that of C0. Greater mass loss indicates poorer wear resistance [28–30].

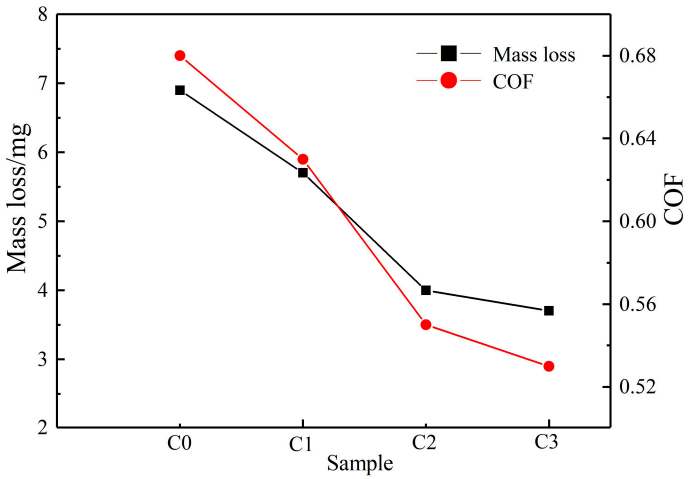

Figure 7. Variation in average COF and mass loss of coatings at different quenching temperatures.

These results indicate that increasing the quenching temperature significantly improved the wear resistance of the coatings. The improvements are attributed to the disappearance of eutectic structures, the increased formation of Mo_2FeB_2 hard phase particles, and the strengthening of the binder phase.

Figure 8 shows the wear morphologies of the coatings at different quenching temperatures. In Figure 8a, the wear surface of the C0 coating exhibits deep, "granular" spalling pits (point I), along with shallower, "flaky", peeling pits (point II), which are associated with the fracture and detachment of eutectic structures. After quenching at 850 °C (Figure 8b), the number of spalling pits slightly decreased, and some evolved into elongated or short bone-shaped pits (point III). These morphological changes suggest that the eutectic structure plays a critical role in determining the coating's wear resistance. At higher quenching temperatures (C2 and C3), the number of spalling pits decreased significantly. In Figure 8c, for the C2 coating, only a few spalling pits and some black oxides (point IV) can be observed. The C3 coating in Figure 8d exhibits the fewest spalling features, indicating an excellent wear performance.

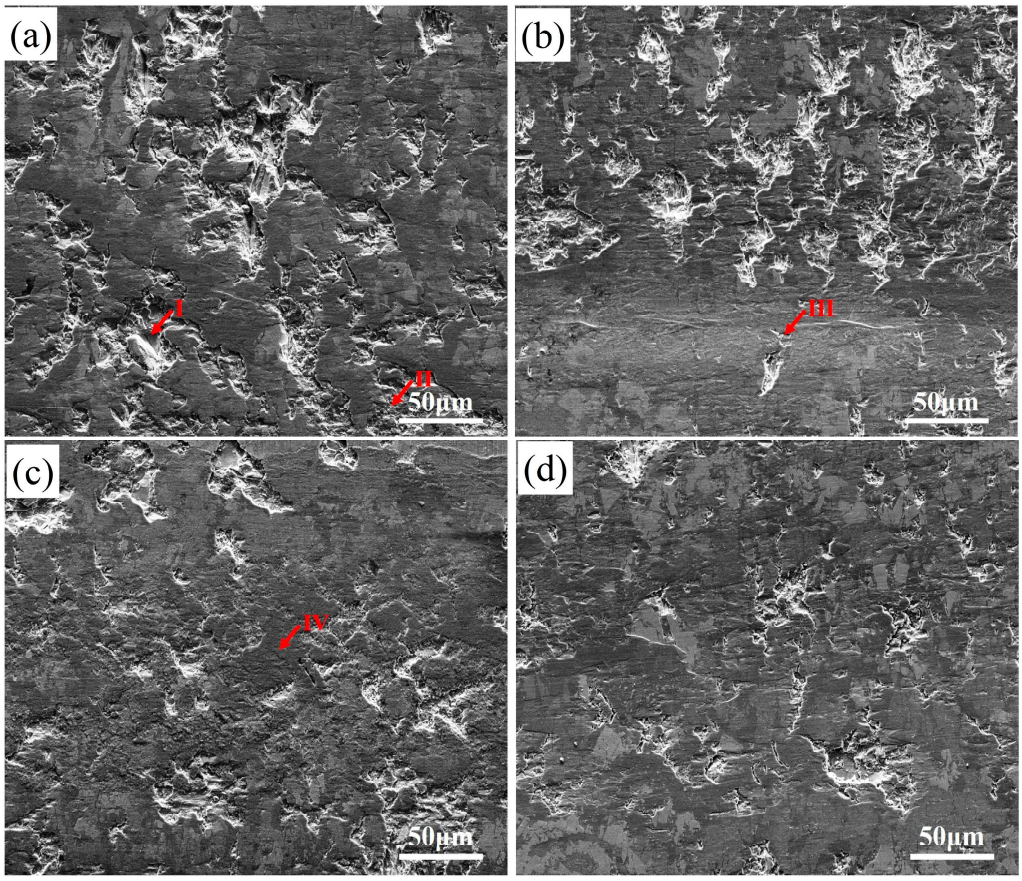

Figure 8. Wear morphologies of coating at different quenching temperatures (**a**) C0; (**b**) C1; (**c**) C2; and (**d**) C3.

In plasma spray-welded coatings, the Mo_2FeB_2 hard phase particles and the eutectic structures possess higher hardness than the α-Fe binder phase, creating a distinct hardness contrast within the microstructure. While the binder phase provides mechanical support, it is more susceptible to wear and tends to generate abrasive debris. During wear, Mo_2FeB_2 hard phases may protrude above the worn surface, and under the shear stress of the Si_3N_4 counter body, these bulging particles can become detached, forming deeper spalling pits. Additionally, the eutectic structure, being brittle due to boron carbide components, is easily fractured and peeled off during wear. However, because boron carbide exhibits hardness

and thermal stability, it does not adhere to the Si_3N_4 ball. Instead, the fractured boron carbide and Mo_2FeB_2 particles are gradually removed from the surface by reciprocating motion, without forming pronounced grooves or plowing tracks.

On the one hand, the disappearance of eutectic structures and the increased formation of Mo_2FeB_2 hard phases after high-temperature quenching significantly enhance wear resistance. The binder phase in the C2 and C3 coatings primarily consists of Fe and Cr and lacks high-temperature-resistant elements such as Ni or Si. As a result, the binder phase is prone to oxidation during wear, leading to the formation of an oxide layer on the worn surface. This oxide layer, gradually formed and distributed by the reciprocating Si_3N_4 friction pair, acts as a lubricant [31], thereby improving wear resistance [32]. Once this oxide layer is completely worn off, broader plowing marks may appear, leveling the worn surface and causing the limited spalling of the hard phases. On the other hand, the increased and evenly distributed Mo_2FeB_2 hard phases in quenched coatings contribute to dispersion strengthening and serve as an anti-wear skeleton. These hard phases mitigate the plowing action of wear debris and abrasives, reduce the fracture of hard phase particles, and protect the worn surface, thereby further enhancing the wear resistance of the coating [21]. In summary, the primary wear mechanism of the coating is abrasive wear resulting from the detachment of hard phase particles.

4. Conclusions

This study aimed to enhance the hardness and wear resistance of H13 alloy steel by fabricating Mo_2FeB_2-based ternary boride coatings through plasma spray welding, followed by quenching at different temperatures. The coating was successfully prepared with a defect-free surface without pores, inclusions, and cracks and a good metallurgical bond with the H13 alloy steel substrate. The main phases in the coating were identified as α-Fe, Mo_2FeB_2, $(Mo,Fe,Cr)_3B_2$, and $Fe_{23}(B,C)_6$.

The morphology of the Mo_2FeB_2 hard phase particles remained relatively unchanged across different quenching temperatures. However, high-temperature quenching (1000 °C and 1150 °C) led to the formation of more Mo_2FeB_2 particles and the gradual disappearance of the reticulated eutectic structure. Both the eutectic structure and the Mo_2FeB_2 hard phase were the key factors influencing the microhardness and wear resistance of the coating.

Microhardness increased progressively with quenching temperature, reaching 1092 $HV_{0.5}$ at 1150 °C (32% higher than that of the as-sprayed coating). Concurrently, the average coefficient of friction (COF) and wear mass loss decreased by 46.4%, demonstrating superior wear resistance in the quenched coatings.

The wear mechanism was primarily abrasive wear caused by the detachment of Mo_2FeB_2 hard phase particles from the coating. The overall wear resistance was significantly enhanced due to the hardness of the Mo_2FeB_2 phase, the increased strength of the binder phase, and the lubricating effect of oxides formed from the binder during wear.

Author Contributions: Conceptualization, H.Z. and Y.Z.; methodology, H.Z.; formal analysis, H.Z., Y.H. and Y.Z.; investigation, H.Z.; writing—original draft preparation, H.Z., Y.H. and Y.Z.; writing—review and editing, Y.Z.; funding acquisition, H.Z. All authors have read and agreed to the published version of the manuscript.

Funding: This research was funded by the PhD research startup foundation of Zhejiang Industry & Trade Vocational College, grant number YJRC202304.

Data Availability Statement: Data will be available upon reasonable request.

Conflicts of Interest: The authors declare no conflicts of interest.

References

1. Hao, J.; Hu, F.; Le, X.; Liu, H.; Yang, H.; Han, J. Microstructure and high-temperature wear behaviour of Inconel 625 multi-layer cladding prepared on H13 mould steel by a hybrid additive manufacturing method. *J. Mater. Process. Technol.* **2021**, *291*, 117036. [CrossRef]
2. Zhang, J.; Yu, M.; Li, Z.; Liu, Y.; Zhang, Q.; Jiang, R.; Sun, S. The effect of laser energy density on the microstructure, residual stress and phase composition of H13 steel treated by laser surface melting. *J. Alloys Compd.* **2021**, *856*, 158168. [CrossRef]
3. Yang, C.; Jing, C.; Fu, T.; Lin, T.; Guo, W.; Liu, N. Effect of TiC addition on the microstructure and properties of laser cladding Ni60A coatings on H13 steel surface. *Mater. Today Commun.* **2024**, *38*, 107904. [CrossRef]
4. Zong, H.; Kang, N.; El Mansori, M. Impact of applied loads on wear mechanisms in H13 steel at various preheating temperatures during laser powder bed fusion additive manufacturing. *Wear* **2024**, *556–557*, 205538. [CrossRef]
5. Lu, H.F.; Xue, K.N.; Xu, X.; Luo, K.Y.; Xing, F.; Yao, J.H.; Lu, J.Z. Effects of laser shock peening on microstructural evolution and wear property of laser hybrid remanufactured Ni25/Fe104 coating on H13 tool steel. *J. Mater. Process. Technol.* **2021**, *291*, 117016. [CrossRef]
6. Pedroso da Silva, S.; Abrão, A.M.; Rodrigues da Silva, E.; Câmara, M.A. Surface modification of AISI H13 steel by die-sinking electrical discharge machining and TiAlN coating: A promising hybrid technique to improve wear resistance. *Wear* **2020**, *462–463*, 203509. [CrossRef]
7. Meng, C.; Cao, R.; Li, J.; Geng, F.; Zhang, Y.; Wu, C.; Wang, X.; Zhuang, W. Mechanical properties of TiC-reinforced H13 steel by bionic laser treatment. *Opt. Laser Technol.* **2021**, *136*, 106815. [CrossRef]
8. Narvan, M.; Ghasemi, A.; Fereiduni, E.; Elbestawi, M. Laser powder bed fusion of functionally graded bi-materials: Role of VC on functionalizing AISI H13 tool steel. *Mater. Des.* **2021**, *201*, 109503. [CrossRef]
9. Lu, J.Z.; Cao, J.; Lu, H.F.; Zhang, L.Y.; Luo, K.Y. Wear properties and microstructural analyses of Fe-based coatings with various WC contents on H13 die steel by laser cladding. *Surf. Coat. Technol.* **2019**, *369*, 228–237. [CrossRef]
10. Mao, X.; Zhu, P.; Sun, X.; Huang, S.; Xu, C.; He, H.; Chen, Y.; Cheng, Z. Nucleation mechanism, particle shape and strengthening behavior of (Ti, Nb) (C, N) particles in Fe-based composite coatings by plasma spray welding. *Ceram. Int.* **2024**, *50*, 27296–27304. [CrossRef]
11. Mao, X.; Zhu, P.; Sun, X.; Xu, C.; Huang, S.; He, H.; Cheng, Z. Effect of N on microstructure, nucleation mechanism and mechanical performance of (Ti, Nb) C particles in Fe-based composite coating via plasma spray welding. *Surf. Coat. Technol.* **2024**, *490*, 131177. [CrossRef]
12. Zhang, L.; Gao, Y.; Huang, Z.; Ma, H.; Liu, Y.; Jie, W.; Zhou, L. Effect of Ni content on the corrosion behavior of Mo2NiB2–Ni cermet in H2SO4 solution. *Ceram. Int.* **2023**, *49*, 36289–36298. [CrossRef]
13. Zhang, L.; Huang, Z.; Jie, W.; Cao, Z.; Liu, Y.; Zhou, L. Effect of impact angle on wear behavior of Mo2NiB2–Ni cermets with different Ni content. *Ceram. Int.* **2022**, *48*, 16944–16955. [CrossRef]
14. Zhang, H.; Pan, Y.; Zhang, Y.; Lian, G.; Cao, Q.; Yang, J. Influence of laser power on the microstructure and properties of in-situ NbC/WCoB–TiC coating by laser cladding. *Mater. Chem. Phys.* **2022**, *290*, 126636. [CrossRef]
15. Zhu, X.; Pan, Y.; Zhang, H.; Ke, D. Effect of Ni content on the microstructure and properties of WCoB-TiC cermets. *Int. J. Refract. Met. Hard Mater.* **2023**, *117*, 106381. [CrossRef]
16. Zhang, H.; Zhang, Y. In-situ synthesized WC reinforcement phase on microstructural evolution, toughness and tribological properties of Mo2FeB2-based composite coatings fabricated by laser cladding. *J. Mater. Res. Technol.* **2025**, *34*, 677–690. [CrossRef]
17. Zhang, Y.; Zhang, H. Influence of laser remelting on the microstructure and properties of Mo2FeB2 ternary boride coatings prepared by laser cladding. *Mater. Today Commun.* **2024**, *41*, 110548. [CrossRef]
18. Lang, X.-Y.; Zhang, G.-H. Microstructure and mechanical properties of Mo2FeB2-316SS cermets prepared by vacuum sintering. *J. Alloys Compd.* **2025**, *1027*, 180626. [CrossRef]
19. Li, B.; Zheng, Y.; Shao, X.; Li, K.; Xu, X.; Chen, M.; Liang, H.; Yang, M. Growth kinetics of ceramic grains during liquid phase sintering in Mo2FeB2-based cermets. *Int. J. Refract. Met. Hard Mater.* **2023**, *110*, 105991. [CrossRef]
20. Cao, Z.; Jian, Y.; Zhao, Z.; Xiao, P.; Xu, L.; Huang, Z. Effect of V doping on the microstructure and mechanical properties of Mo2FeB2-based cermets and investigation on the enhancement mechanism. *J. Alloys Compd.* **2023**, *931*, 167545. [CrossRef]
21. Wei, X.; Chen, Z.; Zhong, J.; Xiang, Y. Feasibility of preparing Mo2FeB2-based cermet coating by electrospark deposition on high speed steel. *Surf. Coat. Technol.* **2016**, *296*, 58–64. [CrossRef]
22. Duan, S.; Ren, W.; Lei, W.; Wang, Y. Study on the microstructure and properties of rail cladding layer after laser quenching. *J. Manuf. Process.* **2023**, *108*, 180–193. [CrossRef]
23. Chen, C.; Feng, A.; Liu, B.; Wei, Y.; Song, X. Effect of quench-tempering and laser quenching on the microstructure and properties of high-chromium cast iron. *J. Mater. Res. Technol.* **2022**, *19*, 2759–2773. [CrossRef]
24. Sun, H.; Ding, H.; Liu, T. Unveiling the effect of vacuum heat treatment on HVOF-sprayed high entropy cantor alloy coatings: Microstructure, diffusion behavior and mechanical property. *J. Mater. Res. Technol.* **2024**, *33*, 9033–9043. [CrossRef]

25. Li, B.; Tian, M.; Feng, L.; Wu, D.; Guo, H.; Gao, Y.; Xu, Y.; An, C.; Liang, C. Effect of heat treatment on the microstructure and mechanical properties of TiAl alloys. *J. Mater. Res. Technol.* **2024**, *33*, 8545–8554. [CrossRef]
26. Xiao, G.; Jiang, J.; Wang, Y.; Liu, Y.; Zhang, Y.; Huang, M. Microstructure and mechanical properties of thixoformed GH4037 parts before and after heat treatment. *Mater. Sci. Eng. A* **2021**, *815*, 141304. [CrossRef]
27. Kuroda, P.A.B.; de Mattos, F.N.; Grandini, C.R.; Afonso, C.R.M. Influence of the heat treatment temperature on the MAO coating produced in the Ti–25Ta–25Zr alloy. *J. Mater. Res. Technol.* **2023**, *26*, 3881–3892. [CrossRef]
28. Zhang, G.; Liu, W.; Bian, H.; Xi, W.; Zhang, K.; Wang, H. A novel approach to enhance the wear resistance of laser-cladded Tribaloy T-800 coatings on DD5 single crystal alloys by addition of Si. *Mater. Charact.* **2025**, *221*, 114728. [CrossRef]
29. Qin, J.; Shu, L.; Wang, J.; Li, P.; Li, A.; Huang, T.; Shi, J.; Qiu, Y.; Dong, H. Study on the preparation and wear properties of laser cladded Incoel718/WC gradient composite coatings. *Mater. Today Commun.* **2024**, *41*, 111080. [CrossRef]
30. Zhang, G.; Liu, W.; Bian, H.; Wang, H.; Wang, W.; Xu, X.; Liu, J. Effect of laser energy density on cracking susceptibility and wear resistance of laser-clad tribaloy T-800 coatings on DD5 single-crystal alloys. *Mater. Today Commun.* **2024**, *40*, 109604. [CrossRef]
31. Belov, D.S.; Blinkov, I.V.; Sergevnin, V.S.; Smirnov, N.I.; Volkhonskii, A.O.; Bondarev, A.V.; Lobova, T.A. Abrasive, hydroabrasive, and erosion wear behaviour of nanostructured (Ti,Al)N-Cu and (Ti,Al)N-Ni coatings. *Surf. Coat. Technol.* **2018**, *338*, 1–13. [CrossRef]
32. Yang, F.; Su, B.; Zhang, A.; Meng, J.; Han, J.; Wu, Y. Tribological properties and wear mechanisms of Mo2FeB2 based cermets at high temperatures. *Tribol. Int.* **2018**, *120*, 391–397. [CrossRef]

Disclaimer/Publisher's Note: The statements, opinions and data contained in all publications are solely those of the individual author(s) and contributor(s) and not of MDPI and/or the editor(s). MDPI and/or the editor(s) disclaim responsibility for any injury to people or property resulting from any ideas, methods, instructions or products referred to in the content.